Optics Letters

High-speed spatially re-modulated structured illumination microscopy

Shijie Tu,[1,2] Xiaoyan Li,[1] Yueying Wang,[1] Wenwen Gong,[1] Xin Liu,[1] Q. Liu,[3] Yubing Han,[1] Cuifang Kuang,[1,3,4] Xu Liu,[1] and Xiang Hao[1,2,*]

[1]College of Optical Science and Engineering, Zhejiang University, Hangzhou 310027, China
[2]Intelligent Optics & Photonics Research Center, Jiaxing Research Institute Zhejiang University, Jiaxing 314000, China
[3]Zhejiang Lab, Research Center for Intelligent Chips and Devices, Hangzhou 311121, China
[4]ZJU-Hangzhou Global Scientific and Technological Innovation Center, Hangzhou 311200, China
*haox@zju.edu.cn

Received 6 February 2023; revised 10 March 2023; accepted 2 April 2023; posted 3 April 2023; published 3 May 2023

Structured illumination microscopy (SIM) allows non-invasive visualization of nanoscale subcellular structures. However, image acquisition and reconstruction become the bottleneck to further improve the imaging speed. Here, we propose a method to accelerate SIM imaging by combining the spatial re-modulation principle with Fourier domain filtering and using measured illumination patterns. This approach enables high-speed, high-quality imaging of dense subcellular structures using a conventional nine-frame SIM modality without phase estimation of the patterns. In addition, seven-frame SIM reconstruction and additional hardware acceleration further improve the imaging speed using our method. Furthermore, our method is also applicable to other spatially uncorrelated illumination patterns, such as distorted sinusoidal, multifocal, and speckle patterns.

https://doi.org/10.1364/OL.485929

Over the past two decades, super-resolution fluorescence microscopy techniques [1–4] have overcome the classical diffraction limit, enabling non-invasive visualization of nanoscale subcellular structures. Among them, structured illumination microscopy (SIM) is notable in live-cell imaging due to its low excitation intensity, fast wide-field imaging, and compatibility with most fluorescent labeling protocols.

Typically, SIM replaces the uniform illumination of a conventional wide-field microscope with a spatially modulated pattern. The non-uniform pattern shifts the unobservable high-frequency components of the sample into the detection passband of the microscope. To reconstruct a super-resolution image with nearly isotropic lateral resolution, a series of raw images of the sample are acquired sequentially as the phase and orientation of the patterns change. Multi-frame acquisition slows down the imaging and dramatically increases the exposure dose. Worse still, post-reconstruction algorithms based on the conventional Wiener-SIM architecture [4–9] are typically complex and time-consuming because the illumination pattern parameters must be accurately estimated, otherwise the results are prone to artifacts. Therefore, applications requiring real-time SIM imaging are severely limited.

There have been several techniques to improve the overall speed of SIM. To reduce the number of raw frames required and thus improve image acquisition speed, some spatial domain iterative algorithms [10,11] and Fourier domain reconstruction algorithms [12,13] have been developed. However, these algorithms are inherently time-consuming and the reconstructed results are sensitive to artifacts. Deep learning SIM reconstruction for frame reduction [14,15] is an alternative, but the "black box" nature makes it difficult to guarantee stable and reliable results. Alternatively, to improve the reconstruction speed, spatial domain reconstruction with simplified workflow [16,17] has been applied to high-speed SIM reconstruction. For example, JSFR-SIM [17] runs 2.8 times faster than conventional Wiener-SIM [5] in the same central processing unit (CPU) environment by using a pre-generated structured coefficient matrix. However, it still requires pre-estimation of the illumination parameters. In addition, additional hardware acceleration such as graphics processing unit (GPU)-based parallel computing [17–19] has been used for real-time SIM imaging.

To improve the overall speed of SIM, we propose spatially re-modulated structured illumination microscopy. By combining a spatial re-modulation principle with Fourier domain filtering and using measured illumination patterns, our approach enables high-speed, optically sectioned, super-resolution, and artifact-free imaging of dense subcellular structures.

The principle of spatial re-modulation can be described as follows: the measured fluorescence signal $M_\ell(\mathbf{r})$ at position $\mathbf{r}$ and frame ℓ is given by the convolution of the intensity-modulated fluorescence source distribution $\rho(\mathbf{r})\cdot I_\ell(\mathbf{r})$ and the detection point spread function (PSF) $h(\mathbf{r})$:

$$M_\ell(\mathbf{r}) = [\rho(\mathbf{r}) \cdot I_\ell(\mathbf{r})] \otimes h(\mathbf{r}), \tag{1}$$

where $\rho(\mathbf{r})$ denotes the fluorescence distribution of the sample, and $I_\ell(\mathbf{r})$ represents the intensity of the illumination pattern at position $\mathbf{r}$ and frame ℓ, which is given by

$$I_\ell(\mathbf{r}) = I_0 + \mu I_0 \cos(\mathbf{k}_\theta \mathbf{r} + \varphi_\ell), \tag{2}$$

where I_0, μ, $\mathbf{k}_\theta$, and φ_ℓ are the average intensity, the modulation depth, the frequency vector, and the initial phase of the sinusoidal illumination pattern, respectively. Substituting Eq. (2)

into Eq. (1), we obtain

$$M_\ell(\mathbf{r}) = M_0(\mathbf{r}) + \mu I_0(\rho(\mathbf{r})\cos(\mathbf{k}_\theta \mathbf{r} + \varphi_\ell)) \otimes h(\mathbf{r}), \quad (3)$$

where $M_0(\mathbf{r})$ can be obtained by Eq. (1) with $I_\ell(\mathbf{r}) = I_0$, denoting a wide-field image generated by uniform illumination.

Here, the frame-dependent fluctuation in measurement $M_\ell(\mathbf{r})$, which contains the unobservable high-frequency components of the sample, is then re-modulated with the corresponding frame-dependent fluctuation in pattern $I_\ell(\mathbf{r})$ as

$$\begin{aligned}&[M_\ell(\mathbf{r}) - M_0(\mathbf{r})] \cdot [I_\ell(\mathbf{r}) - I_0] \\ &= (\mu I_0)^2 [(\rho(\mathbf{r})\cos(\mathbf{k}_\theta \mathbf{r} + \varphi_\ell)) \otimes h(\mathbf{r})] \cos(\mathbf{k}_\theta \mathbf{r} + \varphi_\ell) \\ &= (\mu I_0)^2 \mathcal{F}^{-1} \left\{ \begin{matrix} \tilde{\rho}(\mathbf{k})(\tilde{h}(\mathbf{k} - \mathbf{k}_\theta) + \tilde{h}(\mathbf{k} + \mathbf{k}_\theta)) \\ + \exp(i2\varphi_\ell)\tilde{\rho}(\mathbf{k} - 2\mathbf{k}_\theta)\tilde{h}(\mathbf{k} - \mathbf{k}_\theta) \\ + \exp(-i2\varphi_\ell)\tilde{\rho}(\mathbf{k} + 2\mathbf{k}_\theta)\tilde{h}(\mathbf{k} + \mathbf{k}_\theta) \end{matrix} \right\}, \end{aligned} \quad (4)$$

where $\tilde{\cdot}$ denotes the Fourier transform of a given function, $\tilde{h}$ is the optical transfer function (OTF) with the cutoff frequency k_c, and $\mathcal{F}^{-1}$ is the inverse Fourier transform. A detailed derivation of Eq. (4) can be found in Eq. (S3) in Supplement 1. Furthermore, the squared fluctuation in the pattern is given by

$$\begin{aligned}[I_\ell(\mathbf{r}) - I_0]^2 &= [\mu I_0 \cos(\mathbf{k}_\theta \mathbf{r} + \varphi_\ell)]^2 \\ &= \frac{1}{2}(\mu I_0)^2 [1 + \cos(2\mathbf{k}_\theta \mathbf{r} + 2\varphi_\ell)]. \end{aligned} \quad (5)$$

In addition, considering that $\langle \exp(\pm i2\varphi_\ell)\rangle_\ell = 0$ and $\langle \cos(2\mathbf{k}_\theta \mathbf{r} + 2\varphi_\ell)\rangle_\ell = 0$ when $\varphi_\ell = \varphi_1 + (\ell - 1)\pi/N$ ($N = 2$) or $\varphi_\ell = \varphi_1 + 2(\ell - 1)\pi/N$ ($N \geq 3$), where $\langle\cdot\rangle_\ell$ denotes frame averaging, we have a spatially re-modulated image

$$\begin{aligned} M_{\mathrm{SRM}}(\mathbf{r}) &= \frac{\langle [M_\ell(\mathbf{r}) - M_0(\mathbf{r})] \cdot [I_\ell(\mathbf{r}) - I_0]\rangle_\ell}{\left\langle [I_\ell(\mathbf{r}) - I_0]^2 \right\rangle_\ell} \\ &= 2\mathcal{F}^{-1}\{\tilde{\rho}(\mathbf{k})(\tilde{h}(\mathbf{k} - \mathbf{k}_\theta) + \tilde{h}(\mathbf{k} + \mathbf{k}_\theta))\}. \end{aligned} \quad (6)$$

Equation (6) shows that $\boldsymbol{M}_{\mathrm{SRM}}(\mathbf{r})$ refers to a super-resolution image of the sample with effective OTF $[\tilde{h}(\mathbf{k} - \mathbf{k}_\theta) + \tilde{h}(\mathbf{k} + \mathbf{k}_\theta)]$, whose cutoff frequency is extended to $(k_c + |\mathbf{k}_\theta|)$. In the latter case ($N \geq 3$), where $M_0(\mathbf{r})$ and I_0 can be obtained by averaging measurements and patterns, respectively, $\boldsymbol{M}_{\mathrm{SRM}}(\mathbf{r})$ is equivalently obtained by dividing the covariance of measurements and patterns by the variance of patterns.

From Eq. (6), $\boldsymbol{M}_{\mathrm{SRM}}(\mathbf{r})$ can be obtained without measuring the actual values of pattern parameters I_0, μ, $\mathbf{k}_\theta$, and φ_ℓ, implying fast SIM reconstruction without pattern parameter estimation. In addition, calculations are performed directly on each pixel in the spatial domain, which means that the parameters of the pattern can vary spatially. Therefore, this spatial re-modulation super-resolution principle is expected to be applied to more general illumination patterns and to realize high-speed and high-quality super-resolution imaging.

We have discussed the principle of super-resolution along the frequency vector direction. Similarly, we can average $\boldsymbol{M}_{\mathrm{SRM}}(\mathbf{r})$ in different orientations to obtain a nearly isotropic resolution.

Specifically, the flow chart of nine-frame spatially re-modulated SIM is shown in Fig. 1. A total of nine measurements and nine pattern images (three orientations, three phases per orientation with 120° phase difference) are acquired with a fluorescence sample and a mirror sample, respectively. To suppress the unavoidable background and noise in the experiments, we combined the spatial re-modulation principle with Fourier domain filtering. In preparation, we first perform a Wiener

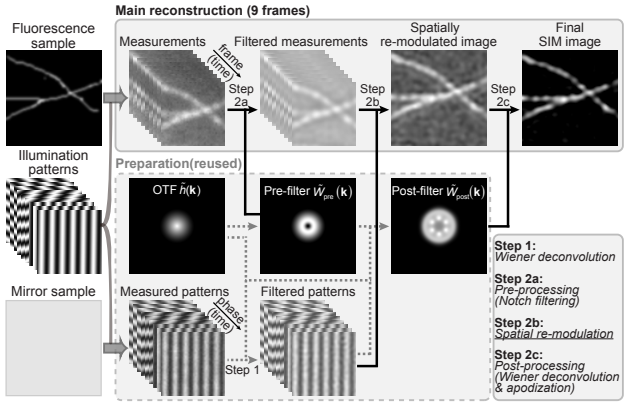

Fig. 1. Flow chart of the nine-frame spatially re-modulated SIM technique. It consists of two parts: the preparation process and the main reconstruction process. The former can be reused for different reconstruction events.

deconvolution on the measured patterns (Step 1) to obtain the illumination patterns. We then generate Fourier filters, such as pre-filter $\tilde{W}_{\mathrm{pre}}(\mathbf{k})$ and post-filter $\tilde{W}_{\mathrm{post}}(\mathbf{k})$, which are used later in the main reconstruction process. During the main reconstruction process, we first preprocess the raw fluorescence images (measurements) with the pre-filter (Step 2a) to suppress high-frequency noise and out-of-focus background caused by sample scattering. We can then use Eq. (6) to obtain the spatially re-modulated image (Step 2b). Finally, we deconvolve the re-modulated image using the post-filter (Step 2c) to improve image contrast and spatial resolution and remove residual background. See Sections 1 and 2 of Supplement 1 for more details on the principle and parameter settings of our method.

To demonstrate the performance of our method, we imaged mitochondria (Fig. 2) in BSC-1 cells, microtubules (Fig. 3), and actin filaments (Fig. S2 in Supplement 1) in COS-7 cells. In this experiment, a custom-built projection SIM setup [20] with an oil objective lens (100×/1.49 TIRF, Nikon) was used. The excitation laser wavelength is 488 nm. The samples were illuminated by sinusoidal patterns (period, 450 nm) with three phase shifts and three orientations. The emission fluorescence with a peak at 525 nm was then collected in reverse by the same objective lens and detected by an scientific CMOS camera (Dhyana 400BSI V2.0, Tucsen). The size of the captured image was 512×512 pixels with a pixel size of 65 nm. More details can be found in Section 3 of Supplement 1.

In Fig. 2(a), the AF488-labeled mitochondria are imaged under wide-field and SIM modes. We quantify the resolution of the images using decorrelation analysis [21]. The resolution in SIM mode is ~146 nm and was consistently roughly 1.85 times better than the resolution in wide-field mode (270 nm). The improved resolution allows a clear distinction of the mitochondrial protein distribution [ROI 1–2 in Fig. 2(b)]. Note that the resolution in wide-field mode is below the Rayleigh criterion (215 nm; calculated as $0.61 \times 525/1.49$) due to the strong low-frequency out-of-focus background. However, the background is reduced in SIM one. As a result, our method achieves a 1.47-fold improvement in resolution relative to the Rayleigh criterion, which is consistent with the theoretical value of 1.48 (calculated as $1 + 215/450$). The reduction of the background benefits from the subtraction of the wide-field image (Step 2b) and pre-processing (Step 2a). Pre-processing is also effective in

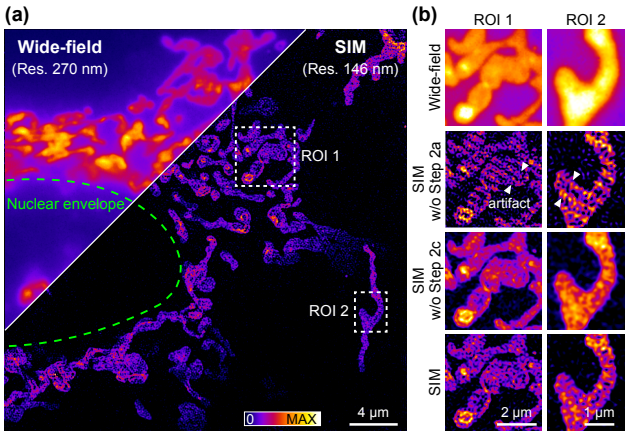

Fig. 2. Mitochondria in BSC-1 cells. (a) Wide-field image (upper left corner) and SIM image. (b) Magnified images of the regions of interest (ROI; white-dashed-box) in panel (a) under wide-field, SIM without Step 2a, SIM without Step 2c, and fully functional SIM modes. All figures are normalized to their peak intensities.

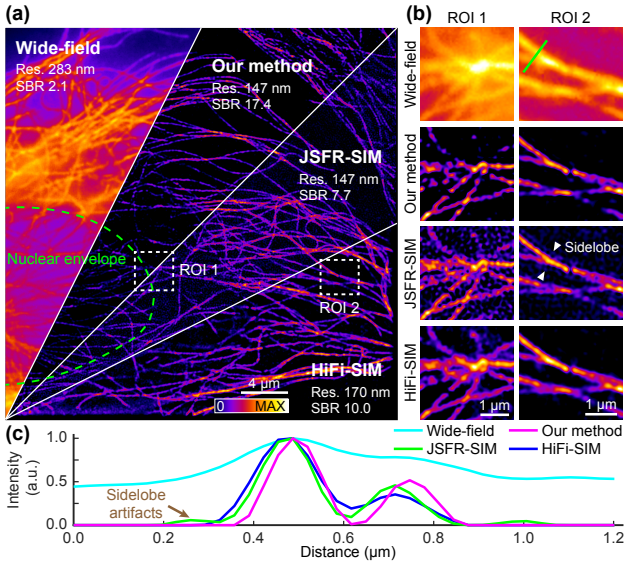

Fig. 3. Microtubules in COS-7 cells. (a) Wide-field image (upper left corner) and the images reconstructed by our method, JSFR-SIM, and HiFi-SIM. (b) Magnified images of the white-dashed-box regions (ROI 1 and ROI 2) in panel (a) under different modes. (c) Intensity profiles along the green line in panel (b).

avoiding periodic artifacts, a general headache in SIM images, caused by out-of-focus backgrounds [6]. To highlight its effect, we compared the results of the SIM mode without Step 2a and the fully functional SIM mode, as shown in Fig. 2(b). Using a similar analysis strategy, we found that the post-processing (Step 2c) helps to further improve the spatial resolution and contrast of the reconstructed images as expected.

We next imaged microtubules (labeled with AF488) and actin filaments (labeled with mEmerald) using wide-field, our method, JSFR-SIM [17], and HiFi-SIM [9] [Fig. 3(a) and Fig. S2 in Supplement 1]. HiFi-SIM is a high-fidelity Wiener-SIM-based algorithm with a two-step spectrum optimization, which demonstrates superior performance compared with previously proposed methods such as fairSIM [7,18] and Hessian-SIM [8]. Although all three methods can be used to obtain relatively close images, we experienced higher background and more sidelobe artifacts in the JSFR-SIM images [Fig. 3(b)], especially in the axially extended regions located near the nuclear envelope (ROI 1 in Fig. 3). However, the resolution of HiFi-SIM is ~15.6% worse than that of JSFR-SIM and our method (170 nm versus 147 nm). Furthermore, our method performs best in terms of signal-to-background ratio (SBR) compared with the other two methods [Fig. 3(a) and Fig. S2 in Supplement 1]. Here, SBR is defined as the ratio of the averaged foreground signal to the averaged background. Therefore, our method exhibits the best performance among the three methods.

In addition to image quality, imaging speed is another major concern for SIM. Compared to other algorithms that typically require nine frames for accurate image reconstruction, our method requires only a minimum of seven frames to achieve comparable results [Eq. (6)]. This configuration facilitates imaging acceleration as fewer frames indicate less acquisition time. To realize this, one wide-field image and six raw SIM images (three orientations, two phases per orientation with 90° phase difference) and their corresponding illumination patterns are acquired.

To investigate whether fewer frames would compromise image quality, we conducted a simulation as shown in Figs. 4(a) and 4(b). Compared to the wide-field mode (resolution $d_R = 215$ nm), our method (resolution $0.59d_R$) provides a 1.7-fold resolution improvement, comparable to HiFi-SIM [9]. We then studied the robustness of the methods to pattern distortions due to optical aberrations [22]. As shown in the bottom row of Fig. 4(b) and Fig. S3 in Supplement 1, the parameters μ, $\mathbf{k}_\theta$, and φ_ℓ of the sinusoidal pattern vary spatially due to the introduced distortion. However, most Wiener-SIM-based algorithms (e.g, HiFi-SIM) require spatially invariant pattern parameters to ensure reliable reconstruction, while our method does not have this limitation [Eq. (6)]. Thus, our method provides the expected convincing reconstruction, while the HiFi-SIM reconstruction deteriorates. Therefore, our method is extremely suitable for complex experiment environments, irrespective of the frame number for image reconstruction.

We also compared the imaging speed of these methods (Table 1). To quantitatively test their effects on reconstruction speed, all algorithms were re-programmed and executed in the same test environment (see Section 6 of Supplement 1 for more details). In a widely used CPU environment, JSFR-SIM [17], our method (9-frame), and our method (7-frame) run 16.6, 16.5, and 20.8 times faster than HiFi-SIM [9], respectively. Reconstruction speed can be further improved by using GPU acceleration. In a GPU environment, our method (7-frame) has the shortest reconstruction time (~6.3 ms), which is 1.62 times faster than that of JSFR-SIM, which has been used for real-time imaging [17]. Furthermore, our method (7-frame) reconstructs a SIM image with fewer raw frames compared with other methods, reducing the image acquisition time and sample exposure dose by a factor of 1.3. Thus, our method (7-frame) has the shortest total imaging time (~30.1 ms), which stems from the advantages of spatial domain reconstruction, phase estimation free, and reduced frames, which are not available in conventional Wiener-SIM-based algorithms [4–9], providing the possibility of a 33-Hz frame rate for real-time SIM imaging.

Notably, the application of our method is not limited to the undistorted or distorted sinusoidal illumination patterns

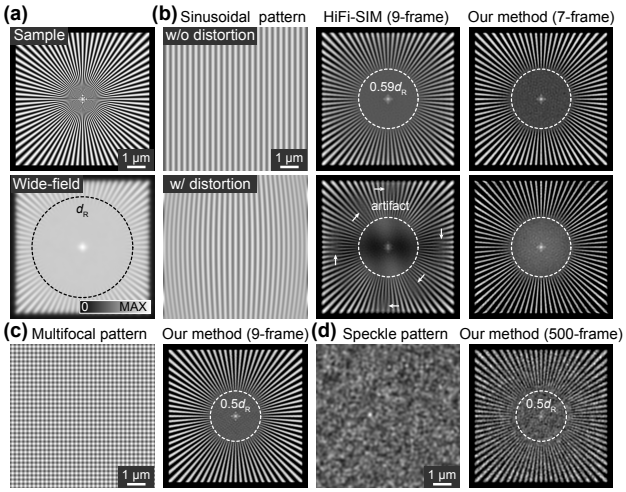

Fig. 4. Simulated reconstructions of a star-like sample illuminated by different patterns. (a) Simulated sample and wide-field image. (b) Undistorted and distorted sinusoidal patterns, and SIM images obtained by HiFi-SIM and our method. (c) Multifocal pattern and SIM image. (d) Speckle pattern and SIM image. d_R is the Rayleigh criterion. See Section 5 of Supplement 1 for more details.

Table 1. Imaging Time for Tested Methods

Method	Acquisition Time (ms)	Reconstruction Time (ms)	
		CPU	GPU
HiFi-SIM	30.6	3587.8 ± 84.0	-
JSFR-SIM	30.6	215.6 ± 13.0	10.2 ± 2.7
Our method (9-frame)	30.6	217.5 ± 6.4	8.6 ± 1.2
Our method (7-frame)	23.8	172.2 ± 4.3	6.3 ± 0.6

described above. Equation (6) implies the potential to combine our method with other spatially uncorrelated patterns. As a demonstration, we performed simulations as shown in Figs. 4(c) and 4(d). The multifocal and speckle patterns were generated as described in Ref. [23]. Reconstructed images with multifocal and speckle illumination have resolutions of 117 nm [Fig. 4(c)] and 131 nm [Fig. 4(d)], which are 1.84 and 1.64 times better than the Rayleigh criterion (215 nm), respectively. In fact, in this case, Eq. (6) gives the covariance of measurements and patterns, showing the super-resolution capacity due to the statistical prior for these patterns, whose values at different positions are not perfectly spatially correlated [23]. In the ideal case where the patterns are perfectly spatially uncorrelated (practically impossible due to band-limited illumination), the effective PSF is a delta function, and thus the sample is reconstructed with a perfect resolution [23]. This case is somewhat similar to single-molecule localization microscopy, where the "illumination pattern" is a stochastic blinking of fluorescent molecules [3,4].

In summary, we have presented a method termed spatially re-modulated SIM to improve the image acquisition and reconstruction speed of SIM. Compared to current state-of-the-art SIM reconstruction methods [9,17], our method provides high-speed, high-quality imaging in biological samples without phase estimation of illumination patterns. We achieve this by combining the spatial re-modulation super-resolution principle with Fourier domain filtering and using measured patterns. Furthermore, this strategy can be applied to other spatially uncorrelated patterns, such as distorted sinusoidal, multifocal, and speckle patterns. Therefore, our method has the advantages of simplicity, low sample exposure, high-speed and high-quality reconstruction, and wide versatility. Thus, our method is adapted to some recently proposed long-term live-cell SIM imaging modalities to realize real-time imaging. Furthermore, our method is also applicable for reconstruction using estimated rather than measured patterns, which improves the generalizability of the technique (Section 7 of Supplement 1).

Funding. National Key R&D Program of China (2022YFB3206000); "Leading Goose" R&D Program of Zhejiang (2022C01077); the Fundamental Research Funds for the Central Universities(2022QZJH29); National Natural Science Foundation of China (92050115); Zhejiang Provincial Natural Science Foundation of China (LZ21F050003).

Acknowledgments. We thank Standard Imaging Biotech for the help of sample preparation and the reviewers for their valuable comments.

Disclosures. The authors declare no conflicts of interest.

Data availability. Code and data underlying the results presented in this paper are available on our GitHub repository [24].

Supplemental document. See Supplement 1 for supporting content.

REFERENCES

1. S. W. Hell and J. Wichmann, Opt. Lett. **19**, 780 (1994).
2. M. J. Rust, M. Bates, and X. Zhuang, Nat. Methods **3**, 793 (2006).
3. E. Betzig, G. H. Patterson, R. Sougrat, O. W. Lindwasser, S. Olenych, J. S. Bonifacino, M. W. Davidson, J. Lippincott-Schwartz, and H. F. Hess, Science **313**, 1642 (2006).
4. M. G. Gustafsson, J. Microsc. **198**, 82 (2000).
5. K. O'Holleran and M. Shaw, Biomed. Opt. Express **5**, 2580 (2014).
6. M. Shaw, L. Zajiczek, and K. O'Holleran, Methods **88**, 11 (2015).
7. M. Muller, V. Monkemoller, S. Hennig, W. Hubner, and T. Huser, Nat. Commun. **7**, 10980 (2016).
8. X. Huang, J. Fan, L. Li, H. Liu, R. Wu, Y. Wu, L. Wei, H. Mao, A. Lal, P. Xi, L. Tang, Y. Zhang, Y. Liu, S. Tan, and L. Chen, Nat. Biotechnol. **36**, 451 (2018).
9. G. Wen, S. Li, L. Wang, X. Chen, Z. Sun, Y. Liang, X. Jin, Y. Xing, Y. Jiu, Y. Tang, and H. Li, Light: Sci. Appl. **10**, 70 (2021).
10. S. Dong, J. Liao, K. Guo, L. Bian, J. Suo, and G. Zheng, Biomed. Opt. Express **6**, 2946 (2015).
11. F. Strohl and C. F. Kaminski, Opt. Lett. **42**, 2511 (2017).
12. A. Lal, C. Shan, K. Zhao, W. Liu, X. Huang, W. Zong, L. Chen, and P. Xi, IEEE Trans. on Image Process. **27**, 4555 (2018).
13. J. Qian, Y. Cao, K. Xu, Y. Bi, W. Xia, Q. Chen, and C. Zuo, Appl. Phys. Lett. **121**, 153701 (2022).
14. L. H. Jin, B. Liu, F. Q. Zhao, S. Hahn, B. W. Dong, R. Y. Song, T. C. Elston, Y. K. Xu, and K. M. Hahn, Nat. Commun. **11**, 1934 (2020).
15. C. N. Christensen, E. N. Ward, M. Lu, P. Lio, and C. F. Kaminski, Biomed. Opt. Express **12**, 2720 (2021).
16. S. Tu, Q. Liu, X. Liu, W. Liu, Z. Zhang, T. Luo, C. Kuang, X. Liu, and X. Hao, Opt. Lett. **45**, 1567 (2020).
17. Z. Wang, T. Zhao, H. Hao, Y. Cai, K. Feng, X. Yun, Y. Liang, S. Wang, Y. Sun, P. R. Bianco, K. Oh, and M. Lei, Adv. Photonics **4**, 1 (2022).
18. A. Markwirth, M. Lachetta, V. Monkemoller, R. Heintzmann, W. Hubner, T. Huser, and M. Muller, Nat. Commun. **10**, 4315 (2019).
19. F. Xu, J. Zhang, D. Ding, W. Liu, C. Zheng, S. Zhou, Y. Chen, and C. Kuang, Opt. Express **30**, 13238 (2022).
20. X. Li, S. Xie, W. Liu, L. Jin, Y. Xu, L. Zhang, X. Hao, Y. Han, C. Kuang, and X. Liu, Opt. Express **29**, 43917 (2021).
21. A. Descloux, K. S. Grussmayer, and A. Radenovic, Nat. Methods **16**, 918 (2019).
22. X. Liu, S. Tu, Y. Xu, H. Song, W. Liu, Q. Liu, C. Kuang, X. Liu, and X. Hao, Front. Phys. **7**, 1 (2020).
23. L. H. Yeh, L. Tian, and L. Waller, Biomed. Opt. Express **8**, 695 (2017).
24. S. Tu, X. Li, Y. Wang, W. Gong, X. Liu, Q. Liu, Y. Han, C. Kuang, X. Liu, and X. Hao, "SRM-SIM," GitHub (2023), https://github.com/Hao-Laboratory/SRM-SIM.